

Plasmon-induced near-field and resonance energy transfer enhancement of photodegradation activity by Au wrapped CuS dual-chain

Jinming Ma, Xiangfu Liu, Rongwen Wang, Feng Zhang, and Guoli Tu (✉)

Wuhan National Laboratory for Optoelectronics, Huazhong University of Science and Technology, Wuhan 430074, China

© Tsinghua University Press 2022

Received: 22 August 2021 / Revised: 30 December 2021 / Accepted: 1 January 2022

ABSTRACT

Self-assembled chain-like nanostructures utilizing localized surface plasmon resonance (LSPR) effect could enhance the local electromagnetic field for energy transfer, which provides huge structural advantages for some transmission-related applications such as photocatalysis. In this work, the dual-chain structure of Au chain wrapped CuS (denoted as Au Chain@CuS) was successfully synthesized by the one-step hydrothermal method. Namely, L-cysteine is used as the sulfur source and linking agent, and copper nitrate is the precursor of copper ions, forming the dual-chain driven by 15 nm uniform Au seeds. Transient absorption spectroscopy (TAS) and finite-difference-time-domain (FDTD) simulation exhibited the highly intensive electromagnetic field around the self-assembly chain, the raised formation and transfer rate of electron-hole pairs between the Au chain and surrounding CuS chain. Meanwhile, it shows an excellent photodegradation activity on dye rhodamine B (RhB). Within 1 h under simulated sunlight, the degradation rate reached 98.81% in Au Chain@CuS, which is 2.27 times higher compared to the bare CuS. The enhanced performance is mainly attributed to the near-field enhancement effect induced by LSPR, as well as the benefits of more effective resonance energy transfer (RET). This research comprehensively shows the electromagnetic field in LSPR metal chain is more intensive by order of magnitude relative to the isolated particles. Simultaneously the continuous CuS chain wrapped outside of the LSPR source effectively absorbs and utilizes the plasmonic energy, then promotes the formation of the photo-generated charge, thus increasing the photocatalytic performance. This founding of wrapped coupled-metal dual-chain provides a promising candidate for the highly efficient photocatalysts.

KEYWORDS

Au Chain@CuS, dual-chain, localized surface plasmon resonance, photodegradation, near-field enhancement, resonance energy transfer

1 Introduction

Rhodamine B (RhB) dye, as a standard basic dye in industry, is widely used in colored glass, mining, steel, and other fields [1–3]. However, it is incredibly harmful to the human body. According to the World Health Organization International Agency for Research on Cancer (IARC) chemical carcinogenic risk assessment: The ingestion of rhodamine dye and skin contact with the substance will cause acute and chronic poisoning. Among numerous degradation technologies, photocatalysis stands out due to the utilization of clean, abundant solar energy and simple equipment demand. However, due to the limitation of the used semiconductors, low light extraction rate, loss, etc., the solar energy conversion efficiency in photocatalytic devices, including photoelectric and photothermal conversion, is still very low [4–7]. For example, TiO₂ has high activity and excellent stability, which becomes the most widely used catalyst. But due to its large bandgap, it can only make use of ultraviolet light that occupies 5% of sunlight, reducing its sunlight utilization rate [8, 9]. Therefore, the construction of an efficient and pollution-free photocatalytic system is imminent.

Integrating a localized surface plasmon resonance (LSPR) metal

nanostructure with a semiconductor is a highly attractive alternative to improve the efficiency of a conventional photocatalytic system [10–13]. The adequately designed architecture allows the formation of LSPR, which originated from the collective oscillation of electromagnetic waves and electrons in the conduction band of noble metals, creating a wide wavelength range of light absorption [14–16]. LSPR profoundly depends on the particle nature, including the composition, size, shape, and interval distance [17–19]. Some physical researches have further shown that metal nanostructures with lightning-rod-like tips generate higher electromagnetic fields at ends and strong coupling generates higher electromagnetic fields at adjacent spots [20–22]. The LSPR simultaneously generates highly energetic electrons through non-radiative decay and facilitates their fast and efficient transfer to the nearby semiconductor, which increases the efficiency of photovoltaic devices by 10%–15% [23–25]. Hence, LSPR metal–semiconductor architecture can reduce many limitations of conventional photocatalysts and enhance photocatalytic activity toward improving the RhB photodegradation.

In recent years, many researchers about the metal-

semiconductor photocatalytic system have been detailed studied. For example, Kavitha et al. provided an in-depth study into the relation between crucial structure-relating features of an Au-ZnO plasmonic photocatalyst such as LSPR effect, charge-carrier dynamics, and surface functionalization, in relation to the photocatalysis [26]. Enhancing the local intensity of the electromagnetic field and the proximity of semiconductors and noble metal are two key factors in maximizing the efficiency of plasmonic metal–semiconductor [27, 28]. On the one hand, the local electromagnetic field distribution of plasmonic metal has spatial inhomogeneity, its intensity of the plasmonic source from the surface decays exponentially. Meanwhile, the closer to the plasmonic source, the more electromagnetic fields can be captured. On the other hand, the hot electrons need overcome the Schottky barrier for escaping from metal to semiconductor at the interface. Thus the increasing distance hinders the resonance energy transfer from metal to semiconductor. Compared to the enhanced electromagnetic field caused by the isolated nanoparticles constructed on the internal or surface of the semiconductor, the self-assembly chain-like collected nanoparticles for energy transfer are more intense. A rational design of plasmonic metal–semiconductor building blocks requires to be implemented. But currently, the related metal–semiconductor building blocks are rarely reported.

The incorporation of the plasmonic metal may promote electromagnetic field amplification, hot-electron injection, and resonant energy transfer (RET), thus improving both light absorption and charge carrier generation in photocatalytic semiconductors [29–31]. LSPR can excite electron–hole pairs in the semiconductor by transferring the concentrated plasmonic energy in localized plasmonic oscillations from the metal to the semiconductor, inducing charge separation in the semiconductor. After the metal nanoparticle obtains the energy of the incident light, the high-energy electrons jump out of the Fermi level of the metal and are on the surface of the nanoparticle. It can hold to dozens of fs, and then quickly injected into the conduction band of the adjacent semiconductor material, which process was known as direct electron transfer (DET). However, the realization of the DET process requires energy level matching. Thus, DET material selection is limited. Additionally, the RET process has also been proposed, which nonradiatively excites electron–hole pairs in the semiconductor through the relaxation of the LSPR dipole through a near-field electromagnetic interaction [32]. RET is similar to Förster resonance energy transfer (FRET) in the near field, where the LSPR dipole replaces the fluorophore [33–35]. Comparatively, it is worthwhile to mention that RET is most efficient to enhance the plasmon-based solar energy conversion efficiency in photocatalysis due to no limitation of electronic band structure matching and charge equilibration. And the RET enhancement is strongly dependent on the proximity of semiconductors and noble metal and the overlap region of the two spectra, which affect the formation rate of electron–hole pairs in the semiconductor [36–40]. Therefore, how to build a superior plasmonic/semiconductor system so as to take advantage of the RET for RhB photodegrading requires careful consideration.

In this work, a dual-chain structure of Au wrapped CuS was successfully fabricated by hydrothermal method, aimed to simultaneously improve near-field enhancement and RET efficiency for facilitating the generation of charge carriers in the semiconductor. The Au Chain@CuS is realized by combining the amino group in L-cysteine with the negative charge on the surface of Au particles, and then the exposed sulfur atoms capture copper ions, self-assembling into a dual-chain by connecting the amino group and the carboxyl group. Under the irradiation of simulated visible light within an hour, the RhB dye degradation rate of Au

Chain@CuS reached 98.81%, which was nearly 2.27 times higher than that of 43.47% in bare CuS. Both the experimental results and theoretical simulation show that the Au chain could strongly induce a higher local electromagnetic field than that of isolated Au nanoparticles. It essentially increases the formation of the electron–hole pair in the nearby CuS. Moreover, the CuS outside could make good use of the RET energy and near-field enhancement provided by the Au chain, converting to the efficient charge separation and high photocatalysis reactivity. Such dual-chain architecture effectively protects the metal nanoparticles from corrosion and achieves a stable RhB degradation performance. This concept of wrapped coupled-metal nanostructure in the CuS chain provides an efficient method to enhance solar energy conversion efficiency.

2 Experimental

2.1 Materials and characterization

Copper nitrate trihydrate ($\text{Cu}(\text{NO}_3)_2 \cdot 3\text{H}_2\text{O}$), L-cysteine, chloroauric acid (HAuCl_4), trisodium citrate ($\text{Na}_3\text{C}_6\text{H}_5\text{O}_7$), RhB, ethyl alcohol, isopropyl alcohol, and acetone were purchased from Sigma–Aldrich Chemical Reagent limited corporation and no more purification treatment before use. Milli-Q deionized (DI) water was used throughout the experiment.

The morphology of the composite system is characterized by transmission electron microscope (TEM). The composite structure is measured by Raman spectrum, X-ray diffraction (XRD), X-ray fluorescence (XRF), and X-ray photoelectron spectroscopy (XPS). The composite system performance is characterized by ultraviolet-visible spectrum (UV), photoluminescence (PL), transient photocurrent responses, electrochemical impedance spectroscopy (EIS). Electron interactions are characterized by transient absorption spectroscopy (TAS). More details were provided in the Electronic Supplementary Material (ESM).

2.2 Synthesis of Au seeds

The Au seeds were synthesized by the Turkevich method [41], 15 mL 1% trisodium citrate was added into boiled 9.71 × 10⁻⁴ mol/L HAuCl_4 aqueous. After 15 min of reaction, cooled down to room temperature naturally. Washed with ethanol and deionized water several times, then centrifuged and kept for later use.

2.3 Synthesis of Au@CuS dual-chain

Au Chain@CuS were synthesized by the one-step hydrothermal method. Primarily, added 2 × 10⁻³ mol $\text{Cu}(\text{NO}_3)_2 \cdot 3\text{H}_2\text{O}$ to the beaker containing 0.08 mol/L L-cysteine, after 0.5 h of vigorous mixing, added 2, 5, and 8 mL Au seeds, respectively, then stirred for half an hour. The mixture in the beaker was added to the reaction kettle and heated at 150 °C for 6 h. After the reaction, the sample was centrifuged several times and placed in a vacuum drying oven at 80 °C overnight. The powder was finely ground and retained for use.

2.4 Finite-difference-time-domain (FDTD) simulation

The electric field intensities and distributions of isolated and coupled nanoparticles were theoretically calculated by FDTD (Lumerical Solutions, Inc.) method using perfectly matched layers (PML) boundary conditions [42]. The geometric radius of Au nanoparticles was set to 7.5 nm as evaluated by TEM results with a decreasing interparticle distance from 10 to 2 nm. The total-field scattered-field (TFSF) at the wavelength of 300–900 nm was selected as a light source along the z direction, and the mesh grid

was set as 0.5 nm. The electric field intensities were monitored by point and plane frequency-domain field monitor. The parameters of Au nanoparticles were used from the software provided. The discussion exhibits the electromagnetic field distributions of Au nanoparticles with different interparticle distances. The intensity enhances at least one order of magnitudes at hot spot area as the distance decrease. It strongly demonstrates that coupled Au can induce more intense localized electric fields when stimulated by appropriate incident light.

2.5 Photodegradation reaction

The reaction of photocatalytic degradation of dyes was conducted in a closed and transparent 25 mL glass bottle. Firstly, added 0.02 g of 0.5%, 1.81%, and 3.07% of the Au@CuS samples to 20 mL of rhodamine dye, mixed for 0.5 h under dark conditions to reach adsorption–desorption equilibrium. The sample was then placed under a 300 W Xenon lamp irradiation, the supernatant was taken every 10 min, centrifuged and subjected to UV absorption measurement, and the degradation rate was calculated according to the UV test results. In addition, 0.02 g of bare CuS powder was used for reference.

3 Results and discussion

Figure 1(a) illustrates the integrated hydrothermal route and formation mechanism of the Au@CuS dual-chain. The realization of this morphology relies on the interaction between the positively charged amino group in L-cysteine and the negative charge on the surface of Au nanoparticles, and then the exposed sulfur atoms of L-cysteine will capture the copper ions, coupling into the dual-chain by connecting the amino group and the carboxyl group (Fig. S1 in the ESM). When a small amount of Au seeds are added, the chain shape cannot be formed, this is due to the fact that the distance between the Au particles is too large for effective coupling. With the continuous addition of Au seeds, the distance between Au seeds gradually shortens, which provides a basis for improving the coupling probability of nanoparticles. Excessive agglomeration will occur when excessive Au particles are added

(Fig. S2 in the ESM). By XRF measurement, the content of Au in these three morphologies of isolated Au with CuS, Au Chain@CuS, and aggregated Au with CuS (denoted as Au Iso@CuS, Au Chain@CuS, and Au Agg@CuS) is 0.5%, 1.81%, and 3.07%, respectively (Fig. S3 in the ESM). Through the Figs. 1(b)–1(d) of TEM images, it can clearly be observed that the chained Au with CuS are successfully synthesized by the self-assembly of moderate Au particles, and each chain is evenly dispersed on the microgrid without aggregation. As seen from Fig. 1(e), there exists a distinct crystal lattices boundary, which belongs to the face-centered cubic (FCC) of Au (111) and the (103) crystal plane of CuS, which strongly proves the formation of this wrapping structure. It can also be macroscopically seen that the Au nanoparticles are uniformly distributed inside of the CuS particles from their energy-dispersive X-ray spectroscopy (EDXS) mapping images.

Figure 2 further confirmed the structure constituent and surface properties of all compounds. Figure 2(a) illustrates that CuS nanoparticles themselves have good crystallinity. It can be seen from XRD that with the addition of Au seeds, there is no Au peak until the Au chain is formed, which shows that the content of Au is minimal, and the ratio of the content of CuS is negligible. Its addition does not change the crystal form of CuS. When excessive Au seeds are added, there is an obvious Au peak at 37.2° corresponds to the (111) crystal plane of Au, which also matches its over-aggregated morphology.

The extinction characteristics of the compound were measured as exhibited in Fig. 2(b). Compared with pure CuS nanoparticles, the addition of Au seeds causes gradual red shifting of the absorption edge, which is provided by the plasmonic absorption of Au nanoparticles. Moreover, it can be intuitively seen that the absorption peaks of Au seeds and pure CuS nanoparticles overlap at 500–650 nm. The larger dipole moment of plasmonic excitation allows a stronger light absorption and energy transfer from Au seeds to the semiconductor.

The results of Raman spectroscopy (Fig. 2(c)) can directly explain the influence of the introduced Au on the field strength

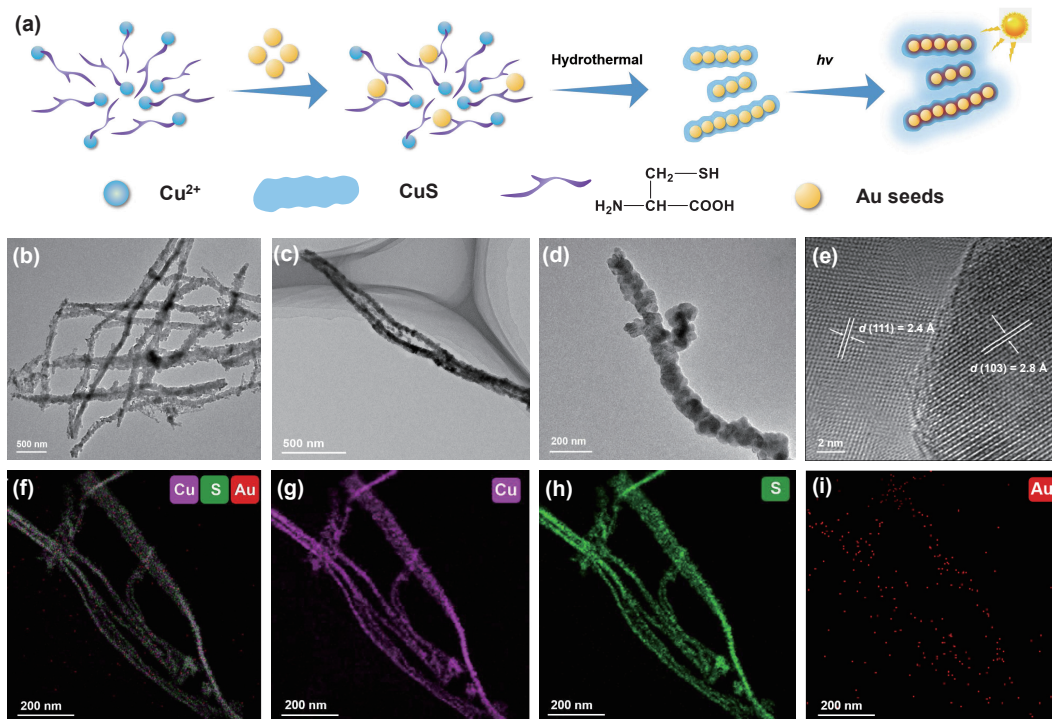


Figure 1 (a) Hydrothermal synthesis route of Au Chain@CuS nanocomposites. (b)–(d) TEM images of nanocomposites with different sizes. (e) Showing the lattice fringes. (f)–(i) High-angle annular dark field (HAADF) and EDXS mapping images of Au Chain@CuS.

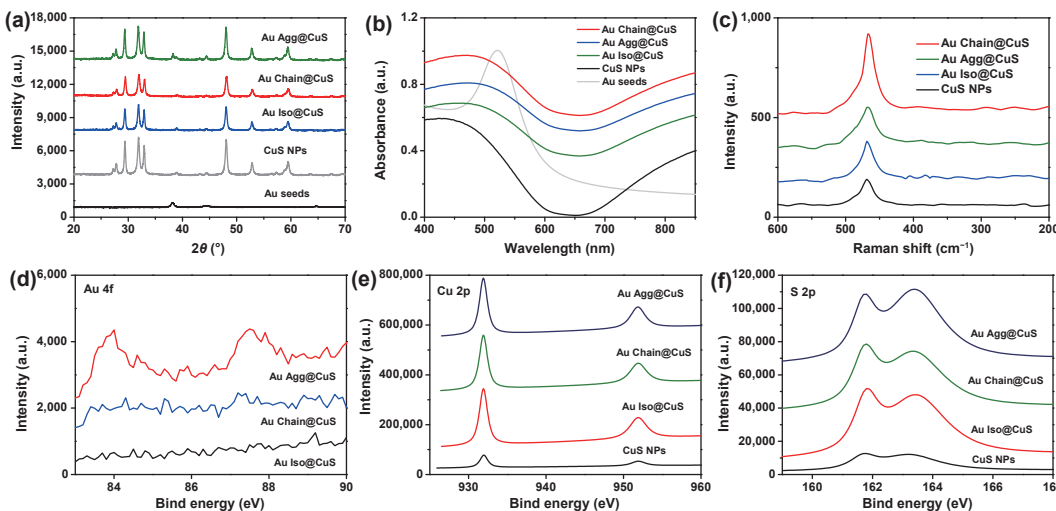


Figure 2 Component structure and surface properties. (a) XRD patterns of Au nanoparticles, CuS nanoparticles, and all Au samples@CuS. (b) UV-Vis spectra, (c) Raman spectra, and (d)–(f) Au 4f, Cu 2p, and S 2p of all samples.

around the semiconductor. The Raman spectrum of bare CuS shows two peaks at 466 and 259 cm⁻¹ [43, 44]. These two peaks are derived from the vibration of the covalent S–S bond and Cu–S bond. Comparably, the Raman signal caused by the vibration of the Cu–S bond is extremely weak compared to the S–S bond, thus the strong peak of S–S bond is generally observed. It can be seen from the Raman spectra that the peak at the S–S bond of the three samples is significantly enhanced after the introduction of Au nanoparticles, and the dual-chain structure has the strongest signal at 466 cm⁻¹, which is due to the CuS receiving the most substantial local electromagnetic field enhancement induced by the adjacent plasmonic Au chain.

XPS results further describe the nature of the surface state of each sample. As plotted in Figs. 2(d)–2(f), the peak positions and intensities of Cu 2p and S 2p orbital from all samples are nearly consistent with Au introduction, which shows that the addition of Au does not change the surface state of CuS. Before the chain formation, there existed no Au peak in Fig. 2(d), which strongly proves the Au chain is completely wrapped in CuS, which dramatically improves the contact area of semiconductor and metal to take full advantage of LSPR. The Au 4f spectrum of 4f_{5/2} and 4f_{7/2}, located at respectively 84.0 and 87.6 eV, stands out when forming the over aggregation morphology. This means that CuS cannot completely wrap the Au chain, and some Au nanoparticles are placed on the surface of CuS when a large amount of Au nanoparticles are added.

The theoretical calculated result by the FDTD method further illustrates the field intensity near the Au chain. It can be observed that the field strength around the Au chain has been increased by order of magnitude when the interparticle distance is reduced from 10 to 2 nm. This is because the electric field intensity around a nanosphere decays exponentially. When the chain is formed, the nanoparticles will collectively oscillate as illuminated, and the electromagnetic field intensity between the nanoparticles will have an additive effect. Plasmon resonance is transferred through electromagnetic waves, which maximizes the field strength of this form. At the same time, the calculated field intensities of the three-particle spacing are shown in Fig. 3(d). As the interparticle distance decreases, the field intensity is significantly improved, and the value changes with the wavelength, which is beneficial to the excitation wavelength selection below. This also fully recognizes the importance and necessity of mastering the synthesis of this morphology technology.

To evaluate the photocatalytic properties of the compound with these three morphologies, the photodegradation of RhB was put

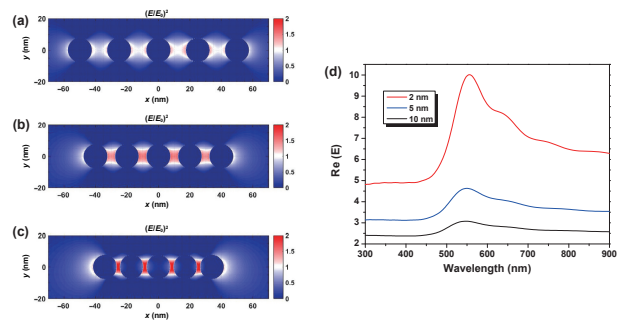


Figure 3 Field intensity distribution with particle spacing of (a) 10 nm, (b) 5 nm, and (c) 2 nm at 530 nm. (d) Field intensity at the wavelength range of 300 to 900 nm.

into effect. Because the change rate of UV absorption value is proportional to the degradation rate, their degradation rate was calculated by comparing the absorption change at 554 nm. As a result, the degradation rates of the Au Iso@CuS, Au Chain@CuS, and Au Agg@CuS reached 57.48%, 98.81%, and 69.72% in 1 h, respectively (Fig. 4(b)). Compared with degradation of 43.47% in pure CuS (Fig. S4 in the ESM), the degradation rate has been significantly improved with the Au incorporation, and Au Chain@CuS is dramatically enhanced 2.27 times. Meanwhile, the stability test of the Au Chain@CuS catalyst was carried out. Under the same conditions, it was found that the degradation rate of 5 cycles (Fig. 4(c)) was basically the same, which also showed that the enhancement of the local electromagnetic field induced by the Au chain did not change the stability of the semiconductor. Meanwhile, measuring the XRD of Au Chain@CuS after five cycles still maintains a good crystallinity (Fig. S5 in the ESM), indicating that it can be reused, which would greatly reduce the industrial cost.

To explore the primary energy transfer mechanism between the dual-chain, the TAS measurement of pure CuS and Au Chain@CuS (Figs. 4(d)–4(f)) is used to characterize the carrier dynamics and relaxation time, then fundamentally confirm the energy transfer mechanism. The sample is made into a dry transparent film, the plasmon is excited with a 100 fs pulse, and the carriers generated in the CuS conduction band are detected. But only the number of electron–hole pairs is related to the wavelength, so $|\Delta T/T|$ is proportional to the number of carriers in the CuS transferred through the plasmon. The carrier lifetimes in the Au Chain@CuS are 163 and 132 ps in bare CuS, which is consistent with inter-band recombination, and the generated carriers are consistent with the overlap integral between the

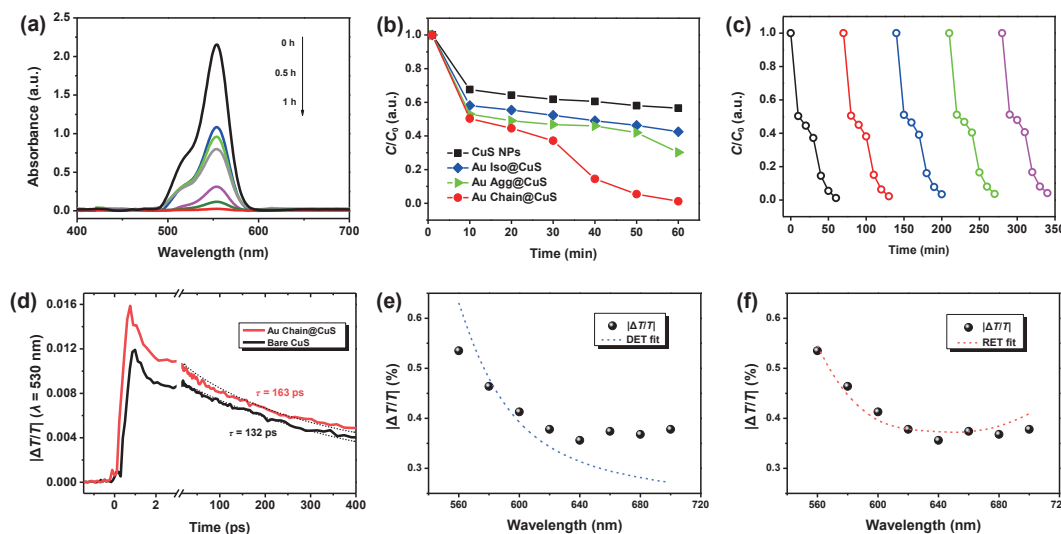


Figure 4 Degradation properties and their fundamental energy transfer mechanism. (a) Variation of rhodamine's UV absorption curves. (b) Degradation rate line graphs of pure CuS and different samples. (c) Five cycle graphs of Au Chain@CuS. (d)–(f) Transient absorption spectra as well as corresponding fitting curves.

plasmonic Au and CuS density of states. In order to confirm that $|\Delta T/T|$ only transmits carrier signals, the average transmission signal in the range of 10–15 ps is extracted (Fig. S6 in the ESM), and the scattering point is formed as a function of wavelength for fitting, leaving only the Gaussian amplitude and the slope related to the flow rate as free parameters. The overlapping function of Au Chain@CuS can be acquired by fitting the overlap parts between LSPR absorption and CuS nanoparticles used by fitting the relative carriers (Fig. S7 in the ESM). The DET fitting completely deviates from the curve, but the RET surface fitting results are in good agreement with the experimental data, which indicates that there is a strong dipole–dipole interaction in Au Chain@CuS, demonstrating that RET process is the primary mechanism of energy transfer from plasmonic Au to CuS. The good overlap between the LSPR band of Au and bandgap absorption of CuS is the prerequisite for RET, which derives from the near-field effect between the LSPR dipole of noble metal and the interband transition dipole of semiconductor.

The photoelectric performance of the Au Chain@CuS was tested and presented in Fig. 5. The PL spectra of all samples have a broad peak (Fig. 5(a)), indicating that the excited electron has multi-radiation processes. With Au incorporated, its PL intensity significantly increased, which also shows that the increased amount of electron–hole pairs recombination and following photon emission. The photocurrent and impedance tests were carried out to further evaluate the charge generation efficiency and the magnitude of the charge transfer resistance. The tests were completed under a three-electrode system. It was found that the Au Chain@CuS exhibited significantly improved transient photocurrent than bare CuS (Fig. 5(b)), which accelerated the photo-induced charges separation, thereby leading to the improvement of photoelectric conversion efficiency. Additionally, Au Chain@CuS shows the smallest arc radius in the impedance curve (Fig. 5(c)), demonstrating its interface transfer resistance is the smallest, matching with its largest degradation rate.

Based on the above analysis, the mechanism of plasmonic Au chain induced photodegradation enhancement was speculated as schematic diagrams in Figs. 5(d) and 5(e). On the one hand, the self-assembled Au chain would provide a stronger near-field enhancement relative to the isolated nanoparticles, providing a secondary light source for CuS on the basis of sunlight and a motivating source for prompting charge separation in CuS. On the other hand, once the incident light excited the LSPR of the Au chain, the RET process from the Au chain to CuS shell would be

activated, and the LSPR dipole of the Au chain would make an interband transition into semiconductor CuS dipole by the near-field effect, which consequently increases the amount of electron–hole pairs for promoting the formation of more OH· radicals. The RET efficiency will increase as the inter-distance between the semiconductor and plasmonic metal in this wrapped structure remarkably decreases. Moreover, the CuS shell was also collected to a chain outside the Au chain, which could take full advantage of the boosts from the plasmonic Au due to the homogeneous distance between RhB and Au. The uniform CuS chain could effectively transfer the additional plasmonic energy to RhB without recombination and quenching (Fig. 5(e)). The synergy of these aspects significantly increases the generation and transfer of electron–hole pairs in the photodegradation process, thereby increasing light dynamic performance.

4 Conclusions

In this paper, a new type of plasmonic source wrapped semiconductor dual-chain catalyst is designed, using the near-field enhancement provided by the plasmonic chain source and the wrapped morphology to shorten the distance between the two to promote more effective energy transfer. It acts on the semiconductor CuS to generate more electron–hole pairs, and the degradation efficiency of the dye rhodamine B reaches 98.81% within one hour, which is close to 100%. Compared with bare CuS nanoparticles, the increase was 2.27 times. Simultaneously, Au nanoparticles are not exposed to the environment to avoid photocorrosion, so that the stability of the composite system can be guaranteed, and a similar performance is still maintained under five cycles. Fully using these unique plasmonic properties of nanostructures to construct metal/semiconductor systems, combining electronic and photonic components in the same device, can be effectively applied in multiple fields.

Acknowledgements

This research was funded by the National Key R&D Program of China (No. 2018YFA0209200).

Electronic Supplementary Material: Supplementary material (general information, experimental section, synthetic procedures, and analytical data) is available in the online version of this article at <https://doi.org/10.1007/s12274-022-4129-5>.

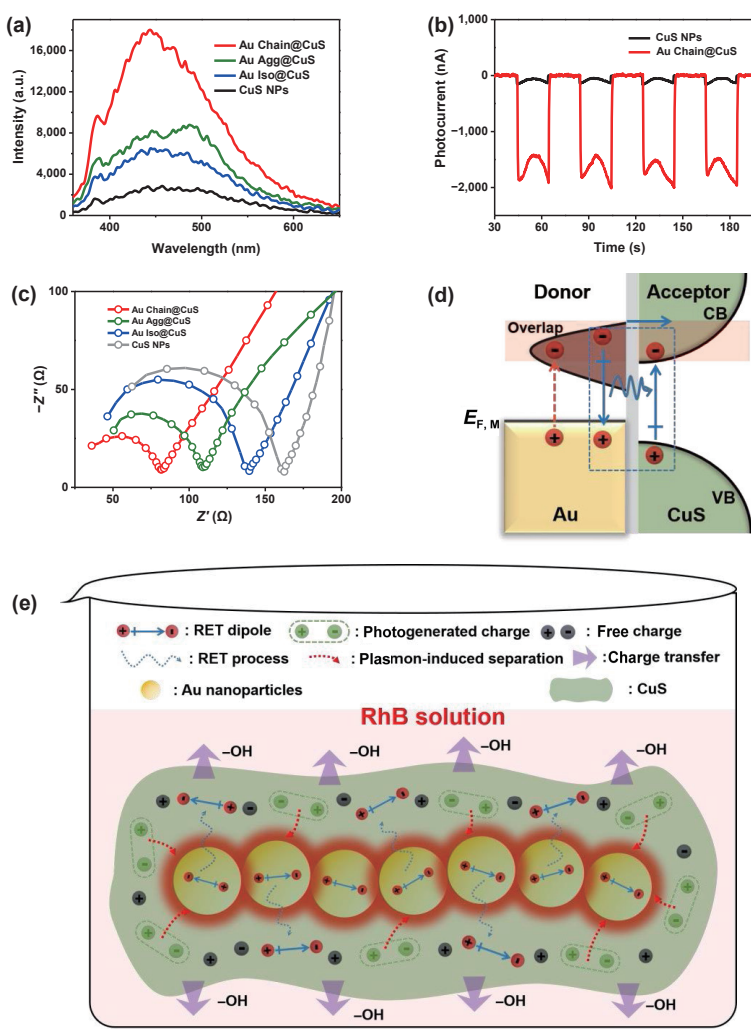


Figure 5 Photoelectric properties and mechanism. (a) PL emission spectra of pure CuS and different Au samples@CuS. (b) Photocurrent response at three electrodes of CuS and Au Chain@CuS samples. (c) Impedance measurement of all samples. (d) RET process mechanism diagram. (e) Photodegradation mechanism diagram of Au Chain@CuS degraded RhB.

References

- [1] Shi, C.; Qi, H. J.; Sun, Z.; Qu, K. Q.; Huang, Z. H.; Li, J.; Dong, M. Y.; Guo, Z. H. Carbon dot-sensitized urchin-like Ti^{3+} self-doped TiO_2 photocatalysts with enhanced photoredox ability for highly efficient removal of Cr^{6+} and RhB. *J. Mater. Chem. C* **2020**, *8*, 2238–2247.
- [2] Liu, N.; Huang, W. Y.; Zhang, X. D.; Tang, L.; Wang, L.; Wang, Y. X.; Wu, M. H. Ultrathin graphene oxide encapsulated in uniform MIL-88A(Fe) for enhanced visible light-driven photodegradation of RhB. *Appl. Catal. B-Environ.* **2018**, *221*, 119–128.
- [3] Anwer, H.; Mahmood, A.; Lee, J.; Kim, K. H.; Park, J. W.; Yip, A. C. K. Photocatalysts for degradation of dyes in industrial effluents: Opportunities and challenges. *Nano Res.* **2019**, *12*, 955–972.
- [4] Gong, J. L.; Li, C.; Wasielewski, M. R. Advances in solar energy conversion. *Chem. Soc. Rev.* **2019**, *48*, 1862–1864.
- [5] Lewis, N. S. Introduction: Solar energy conversion. *Chem. Rev.* **2015**, *115*, 12631–12632.
- [6] Shen, J. X.; Li, Y. Z.; Zhao, H. Y.; Pan, K.; Li, X.; Qu, Y.; Wang, G. F.; Wang, D. S. Modulating the photoelectrons of g-C₃N₄ via coupling MgTi₂O₅ as appropriate platform for visible-light-driven photocatalytic solar energy conversion. *Nano Res.* **2019**, *12*, 1931–1936.
- [7] Xiao, L. H.; Chen, X.; Yang, X. Y.; Sun, J. H.; Geng, J. X. Recent advances in polymer-based photothermal materials for biological applications. *ACS Appl. Polym. Mater.* **2020**, *2*, 4273–4288.
- [8] Lv, Y.; Yue, L.; Khan, I. M.; Zhou, Y.; Cao, W. B.; Niazi, S.; Wang, Z. P. Fabrication of magnetically recyclable yolk-shell Fe₃O₄@TiO₂ nanosheet/Ag/g-C₃N₄ microspheres for enhanced photocatalytic degradation of organic pollutants. *Nano Res.* **2021**, *14*, 2363–2371.
- [9] Meng, D. L.; Fan, J. B.; Ma, J. P.; Du, S. W.; Geng, J. X. The preparation and functional applications of carbon nanomaterial/conjugated polymer composites. *Compos. Commun.* **2019**, *12*, 64–73.
- [10] Chang, Y.; Cheng, Y.; Feng, Y. L.; Jian, H.; Wang, L.; Ma, X. M.; Li, X.; Zhang, H. Y. Resonance energy transfer-promoted photothermal and photodynamic performance of gold-copper sulfide yolk-shell nanoparticles for chemophototherapy of cancer. *Nano Lett.* **2018**, *18*, 886–897.
- [11] Jian, C. C.; Zhang, J. Q.; He, W. M.; Ma, X. C. Au-Al intermetallic compounds: A series of more efficient LSPR materials for hot carriers-based applications than noble metal Au. *Nano Energy* **2021**, *82*, 105763.
- [12] Xu, J.; Yang, W. M.; Huang, S. J.; Yin, H.; Zhang, H.; Radjenovic, P.; Yang, Z. L.; Tian, Z. Q.; Li, J. F. CdS core-Au plasmonic satellites nanostructure enhanced photocatalytic hydrogen evolution reaction. *Nano Energy* **2018**, *49*, 363–371.
- [13] Xue, X. H.; Chen, R. P.; Yan, C. Z.; Zhao, P. Y.; Hu, Y.; Zhang, W. J.; Yang, S. Y.; Jin, Z. Review on photocatalytic and electrocatalytic artificial nitrogen fixation for ammonia synthesis at mild conditions: Advances, challenges and perspectives. *Nano Res.* **2019**, *12*, 1229–1249.
- [14] Yu, T.; Wei, Q. S. Plasmonic molecular assays: Recent advances and applications for mobile health. *Nano Res.* **2018**, *11*, 5439–5473.
- [15] Vu, N. N.; Kaliaguine, S.; Do, T. O. Plasmonic photocatalysts for sunlight-driven reduction of CO₂: Details, developments, and perspectives. *ChemSusChem* **2020**, *13*, 3967–3991.



- [16] Lee, J. B.; Choi, S.; Kim, J.; Nam, Y. S. Plasmonically-assisted nanoarchitectures for solar water splitting: Obstacles and breakthroughs. *Nano Today* **2017**, *16*, 61–81.
- [17] Yuan, L.; Lou, M. H.; Clark, B. D.; Lou, M. H.; Zhou, L. N.; Tian, S.; Jacobson, C. R.; Nordlander, P.; Halas, N. J. Morphology-dependent reactivity of a plasmonic photocatalyst. *ACS Nano* **2020**, *14*, 12054–12063.
- [18] Göeken, K. L.; Schasfoort, R. B. M.; Subramaniam, V.; Gill, R. Spermine induced reversible collapse of deoxyribonucleic acid-bridged nanoparticle-based assemblies. *Nano Res.* **2018**, *11*, 383–396.
- [19] Lin, L.; Chen, M.; Qin, H. Y.; Peng, X. G. Ag nanocrystals with nearly ideal optical quality: Synthesis, growth mechanism, and characterizations. *J. Am. Chem. Soc.* **2018**, *140*, 17734–17742.
- [20] Hooshmand, N.; Mousavi, H. S.; Panikkanvalappil, S. R.; Adibi, A.; El-Sayed, M. A. High-sensitivity molecular sensing using plasmonic nanocube chains in classical and quantum coupling regimes. *Nano Today* **2017**, *17*, 14–22.
- [21] Tira, C.; Tira, D.; Simon, T.; Astilean, S. Finite-difference time-domain (FDTD) design of gold nanoparticle chains with specific surface plasmon resonance. *J. Mol. Struct.* **2014**, *1072*, 137–143.
- [22] Lv, Q.; Gao, M. Y.; Cheng, Z. H.; Chen, Q.; Shen, A. G.; Hu, J. M. Rational synthesis of hollow cubic CuS@Spiky Au core–shell nanoparticles for enhanced photothermal and SERS effects. *Chem. Commun.* **2018**, *54*, 13399–13402.
- [23] Huang, C. L.; Kumar, G.; Sharma, G. D.; Chen, F. C. Plasmonic effects of copper nanoparticles in polymer photovoltaic devices for outdoor and indoor applications. *Appl. Phys. Lett.* **2020**, *116*, 253302.
- [24] Liu, Z. H.; Leow, W. R.; Chen, X. D. Bio-inspired plasmonic photocatalysts. *Small Methods* **2019**, *3*, 1800295.
- [25] Ma, X. C.; Sun, H.; Wang, Y. C.; Wu, X.; Zhang, J. Q. Electronic and optical properties of strained noble metals: Implications for applications based on LSPR. *Nano Energy* **2018**, *53*, 932–939.
- [26] Kavitha, R.; Kumar, S. G. A review on plasmonic Au-ZnO heterojunction photocatalysts: Preparation, modifications and related charge carrier dynamics. *Mater. Sci. Semicond. Process.* **2019**, *93*, 59–91.
- [27] Zhang, J. N.; Hu, W. P.; Cao, S.; Piao, L. Y. Recent progress for hydrogen production by photocatalytic natural or simulated seawater splitting. *Nano Res.* **2020**, *13*, 2313–2322.
- [28] Yu, G. Y.; Qian, J.; Zhang, P.; Zhang, B.; Zhang, W. X.; Yan, W. F.; Liu, G. Collective excitation of plasmon-coupled Au-nanochain boosts photocatalytic hydrogen evolution of semiconductor. *Nat. Commun.* **2019**, *10*, 4912.
- [29] Liang, L.; Zheng, P.; Zhang, C.; Barman, I. A programmable DNA-silicification-based nanocavity for single-molecule plasmonic sensing. *Adv. Mater.* **2021**, *33*, 2005133.
- [30] Cushing, S. K.; Li, J. T.; Meng, F. K.; Senty, T. R.; Suri, S.; Zhi, M. J.; Li, M.; Bristow, A. D.; Wu, N. Q. Photocatalytic activity enhanced by plasmonic resonant energy transfer from metal to semiconductor. *J. Am. Chem. Soc.* **2012**, *134*, 15033–15041.
- [31] Li, J. T.; Cushing, S. K.; Meng, F. K.; Senty, T. R.; Bristow, A. D.; Wu, N. Q. Plasmon-induced resonance energy transfer for solar energy conversion. *Nat. Photonics* **2015**, *9*, 601–607.
- [32] Wu, K.; Chen, J.; McBride, J. R.; Lian, T. Efficient hot-electron transfer by a plasmon-induced interfacial charge-transfer transition. *Science* **2015**, *349*, 632–635.
- [33] Wu, L. L.; Huang, C. S.; Emery, B. P.; Sedgwick, A. C.; Bull, S. D.; He, X. P.; Tian, H.; Yoon, J.; Sessler, J. L.; James, T. D. Förster resonance energy transfer (FRET)-based small-molecule sensors and imaging agents. *Chem. Soc. Rev.* **2020**, *49*, 511–5139.
- [34] Lerner, E.; Cordes, T.; Ingargiola, A.; Alhadid, Y.; Chung, S. Y.; Michalet, X.; Weiss, S. Toward dynamic structural biology: Two decades of single-molecule Förster resonance energy transfer. *Science* **2018**, *359*, eaan1133.
- [35] Jeon, J.; You, D. G.; Um, W.; Lee, J.; Kim, C. H.; Shin, S.; Kwon, S.; Park, J. H. Chemiluminescence resonance energy transfer-based nanoparticles for quantum yield-enhanced cancer phototheranostics. *Sci. Adv.* **2020**, *6*, eaaz8400.
- [36] Singh, M. P.; Strouse, G. F. Involvement of the LSPR spectral overlap for energy transfer between a dye and Au nanoparticle. *J. Am. Chem. Soc.* **2010**, *132*, 9383–9391.
- [37] Tan, S. J.; Argondizzo, A.; Ren, J. D.; Liu, L. M.; Zhao, J.; Petek, H. Plasmonic coupling at a metal/semiconductor interface. *Nat. Photonics* **2017**, *11*, 806–812.
- [38] Xu, R.; Wen, L. Y.; Wang, Z. J.; Zhao, H. P.; Mu, G. N.; Zeng, Z. Q.; Zhou, M.; Bohm, S.; Zhang, H. M.; Wu, Y. H. et al. Programmable multiple plasmonic resonances of nanoparticle superlattice for enhancing photoelectrochemical activity. *Adv. Funct. Mater.* **2020**, *30*, 2005170.
- [39] Li, J. Y.; Dong, X. A.; Sun, Y. J.; Cen, W. L.; Dong, F. Facet-dependent interfacial charge separation and transfer in plasmonic photocatalysts. *Appl. Catal. B-Environ.* **2018**, *226*, 269–277.
- [40] Meng, D. L.; Yang, S. J.; Guo, L.; Li, G. X.; Ge, J. C.; Huang, Y.; Bielawski, C. W.; Geng, J. X. The enhanced photothermal effect of graphene/conjugated polymer composites: Photoinduced energy transfer and applications in photocontrolled switches. *Chem. Commun.* **2014**, *50*, 14345–14348.
- [41] Frens, G. Particle size and sol stability in metal colloids. *Kolloid-Z. u. Z. Polymere* **1972**, *250*, 736–741.
- [42] Jeong, S.; Liu, Y.; Zhong, Y. X.; Zhan, X.; Li, Y. D.; Wang, Y.; Cha, P. M.; Chen, J.; Ye, X. C. Heterometallic seed-mediated growth of monodisperse colloidal copper nanorods with widely tunable plasmonic resonances. *Nano Lett.* **2020**, *20*, 7263–7271.
- [43] Minceva-Sukarova, B.; Najdoski, M.; Grozdanov, I.; Chunnillall, C. J. Raman spectra of thin solid films of some metal sulfides. *J. Mol. Struct.* **1997**, *410–411*, 267–270.
- [44] Jin, P. J.; Yao, Z. Q.; Zhang, M. L.; Li, Y. H.; Xing, H. P. A pigment (CuS) identified by micro-Raman spectroscopy on a Chinese funerary lacquer ware of West Han Dynasty. *J. Raman Spectrosc.* **2010**, *41*, 222–225.